Contract No.:

This manuscript has been authored by Savannah River Nuclear Solutions (SRNS), LLC under Contract No. DE-AC09-08SR22470 with the U.S. Department of Energy (DOE) Office of Environmental Management (EM).

Disclaimer:

The United States Government retains and the publisher, by accepting this article for publication, acknowledges that the United States Government retains a non-exclusive, paid-up, irrevocable, worldwide license to publish or reproduce the published form of this work, or allow others to do so, for United States Government purposes.

Modeling of a thermal energy storage system based on coupled metal hydrides (magnesium iron – sodium alanate) for concentrating solar power plants

d'Entremont A[1], Corgnale C[1,2,*], Sulic M[1,2], Hardy B[1], Zidan R[1], Motyka T[1,2]

1. Savannah River National Laboratory, Aiken, SC, 29808, USA

2. Greenway Energy LLC, Aiken, SC, 29803, USA

Abstract

Concentrating solar power plants represent low cost and efficient solutions for renewable electricity production only if adequate thermal energy storage systems are included. Metal hydride thermal energy storage systems have demonstrated the potential to achieve very high volumetric energy densities, high exergetic efficiencies, and low costs. The current work analyzes the technical feasibility and the performance of a storage system based on the high temperature Mg_2FeH_6 hydride coupled with the low temperature Na_3AlH_6 hydride. To accomplish this, a detailed transport model has been set up and the coupled metal hydride system has been simulated based on a laboratory scale experimental configuration. Proper kinetics expressions have been developed and included in the model to replicate the absorption and desorption process in the high temperature and low temperature hydride materials. The system showed adequate hydrogen transfer between the two metal hydrides, with almost complete charging and discharging, during both thermal energy storage and thermal energy release. The system operating temperatures varied from 450 °C to 500 °C, with hydrogen pressures between 30 bar and 70 bar. This makes the thermal energy storage system a suitable candidate for pairing with a solar driven steam power plant. The model results, obtained for the selected experimental

---

* Corresponding author. Tel: +18036179689; Email: claudio.corgnale@greenway-energy.com

configuration, showed an actual thermal energy storage system volumetric energy density of about 132

kWh/m^3, which is more than 5 times the U.S. Department of Energy SunShot target (25 kWh/m^3).

Nomenclature and abbreviations

Abbreviations

HTMH	High-temperature metal hydride
LTMH	Low-temperature metal hydride
MH	Metal hydride
SOC	State of Charge
SRNL	Savannah River National Laboratory
TES	Thermal energy storage

Variables

c	Molar concentration of H_2 (mol/m^3)
C	Material specific heat (J/kg·K)
C_a	Pre-exponential absorption kinetics factor (s^{-1})
C_d	Pre-exponential desorption kinetics factor (s^{-1})
E_a	Absorption activation energy (J/mol)
E_d	Desorption activation energy (J/mol)
ΔH	Enthalpy of reaction for H_2 desorption (J/mol)
h	Molar enthalpy of H_2 (J/mol)
k	Thermal conductivity (W/m·K)
L	Fill length of MH in test vessel cavity (m)
M_{H2}	Molecular weight of H_2 (kg/g-mol)
n_M	Molar H_2 storage capacity of MH bed (mol)

P	Gas pressure (Pa)
P_{atm}	Atmospheric pressure (Pa)
P_{eq}	Equilibrium pressure between the MH and the gas (Pa)
$\dot{q}$	Volumetric thermal power input (W/m^3)
Q	Thermal energy input (J)
$\dot{Q}$	Thermal power input (W)
R	Universal gas constant (J/mol·K)
R_v	Radius of MH cavity in test vessel (m)
S	Mass rate of production of H$_2$ gas (kg/m^{3}s)
ΔS	Entropy of reaction (J/mol·K)
T	Temperature (K)
t	Time (s)
$\vec{v}$	Gas velocity vector (m/s)
$\vec{v}_s$	Superficial gas velocity vector (m/s)
X	Molar concentration of H$_2$ absorbed within the MH (mol/m^3)
X_m	Minimum molar concentration of H$_2$ in MH (mol/m^3)
X_M	Maximum molar concentration of H$_2$ in MH (mol/m^3)

Greek letters

ε	Porosity of the MH bed
η_d	Dilatational viscosity of H$_2$ gas (Pa·s)
μ	Dynamic viscosity of H$_2$ gas (Pa·s)
ρ	Mass density (kg/m^3)
$\underline{\underline{\tau}}$	Viscous stress tensor (Pa)

Subscripts

$H2$	Associated with H_2 gas
$HTMH$	Associated with high-temperature metal hydride
$LTMH$	Associated with low-temperature metal hydride
MH	Associated with metal hydride (same value for both HTMH and LTMH)
$MHBulk$	Associated with bulk density of the MH material (same value for both HTMH and LTMH)
SS	Associated with stainless steel
0	Initial condition

1   Introduction

Concentrating solar power plants represent one of the best options to produce renewable electricity [1], since they have high potential for providing highly dispatchable power among all the renewable options [2-5]. However, in order to achieve low electricity production costs, concentrating solar power plants need to be equipped with suitable thermal energy storage (TES) systems, allowing for higher plant capacity factors [6]. The storage system enables the power plant to work 24/7 at a power level determined by the plant capacity factor, mainly depending on the storage time and the plant location. Currently, thermal energy can be stored either as sensible heat, or latent heat or thermochemical heat [2-3].

Among the third category, metal-hydride-based TES systems represent a very appealing option showing high efficiencies and low costs [7-8]. During the day, when direct solar power is available, the power plant is driven directly by the available solar power and the surplus heat is stored in the metal hydride (MH) system. During the storage process the high-temperature metal hydride (HTMH) material, working at the temperatures required by the power plant, exchanges heat with the solar heat transfer fluid and releases hydrogen in an endothermic process. The hydrogen is absorbed through an exothermic process in the low-temperature metal hydride (LTMH) material, which rejects the heat at low temperatures. During the night or when direct solar power is not

sufficient, the hydrogen, previously absorbed within the LTMH, is transferred back to the HTMH. The exothermic hydrogen absorption in the HTMH provides the high temperature thermal power required to drive the power plant when direct solar power is unavailable. More details on the principle of the MH-based TES systems can be found in Reference [7,8]. Recent analyses have demonstrated that MH-based TES systems can achieve high volumetric energy densities almost 10 times larger than traditional molten salt systems [7]. In addition, MH-based TES systems have the potential for high exergetic efficiencies (on the order of 95%) and cost often less than the molten salt systems, approaching the U.S. Department of Energy target of 15 $/kWhth [7-9]. Depending on the type of the power plant coupled with the solar system, three classes of metal hydrides can be identified. The first class operates at temperatures on the order of 300-450 °C and can be coupled with traditional steam power plant based on the Hirn cycle. Typical metal hydrides, used to store thermal energy at these temperatures, are based on Mg hydride (e.g. MgH_2 and Mg_2FeH_6) [10-13]. The second class of metal hydrides operates at temperatures on the order of 500-650 °C and can be coupled with high pressure (or supercritical) steam power plants. This class of materials is based on Na hydrides, such as $NaMgH_3$, NaH and the recently developed $NaMgH_2F$ [9,14]. A third class of metal hydrides, working at temperatures on the order of 700-850 °C, can be based on Ti or Ca hydrides. This class of materials is widely being studied as possible TES systems for future high efficiency solar plants, based on sCO2 Brayton cycles [15-16].

The present work focuses on a low cost TES system comprised of Mg_2FeH_6 as the HTMH material, coupled with Na_3AlH_6 as the LTMH material. This coupled system represents one of the best options to store energy in a solar plant that includes a back pressure steam power plant, operating at temperatures on the order of 400-450 °C. Mg-Fe hydride has been demonstrated to be one of the less expensive available metal hydrides operating at this range of temperatures [7]. Among the LTMH materials, other compounds (based on rare earth materials, or Ti materials) have been extensively modeled and studied experimentally in the past [17,18,19]. It has also been shown that these materials have the right properties to operate as coupled TES materials [7]. However their cost is at least on the order of three times higher than the Na_3AlH_6 material cost [7]. The TES system consisting of

Mg_2FeH_6 coupled with Na_3AlH_6 can reach a cost of about 33 $/kWhth, and exergetic efficiencies higher than 70% at 530 °C [7,15]. However, the actual technical feasibility of the proposed system (i.e. the effective hydrogen exchange between the two materials with energy storage and release) has never previously been demonstrated. In the past, only a very few coupled MH systems have been demonstrated pairing (more traditional) MgH_2 HTMH material with high pressure gas hydrogen tank or expensive Rare Earth hydride based LTMH materials [10-,11]. The objective of this work is to demonstrate the technical feasibility of the proposed system (Mg_2FeH_6 coupled with Na_3AlH_6) from a numerical modeling perspective under specific operating conditions. To accomplish this objective a detailed transport model has been developed accounting for mass, energy and momentum balance, as well as kinetics expressions for the two MH materials. Results are presented and discussed showing temperature, pressures and hydrogen concentration profiles for the two coupled metal hydrides. A discussion on the actual volumetric energy density achieved in a laboratory scale TES system is also included. The results obtained from the simulation will be used to guide the future laboratory scale experimental tests and to identify the optimum operating conditions for the integrated solar power plant at larger scales.

2 Methods and Analysis

2.1 Numerical model

A detailed transport model has been developed to simulate the TES system based on coupled metal hydrides. The model is comprised of mass, momentum and energy balance equations, with additional ancillary equations to evaluate the properties of the gaseous hydrogen. Suitable kinetics expressions have also been included to simulate the charging and discharging process for the HTMH and the LTMH. The model has been developed using a finite element analysis approach and the differential equations have been solved using COMSOL Multiphysics®.

2.1.1 Transport model constitutive equations

The differential equation of the mass balance for hydrogen in gaseous state within the porous materials is expressed as follows:

$$\varepsilon \frac{\partial \rho}{\partial t} + \nabla \cdot \left(\rho \vec{v}_s \right) = -S \qquad (1)$$

with ρ being the density of the H_2 gas, ε being the porosity of the MH bed, $\vec{v}_s = \varepsilon \vec{v}$ being the superficial gas velocity. The mass rate of hydrogen gas consumption (positive during hydrogen absorption/MH charging) is expressed as:

$$S = M_{H2} \frac{\partial X}{\partial t} \qquad (2)$$

with M_{H2} being the molecular weight of hydrogen and X being the local concentration of H_2 absorbed within the metal hydride.

The mass balance equation of hydrogen flowing in the free volume without porous media and without mass sources has the following expression:

$$\frac{\partial \rho}{\partial t} + \nabla \cdot \left(\rho \vec{v} \right) = 0 \qquad (3)$$

The differential form of momentum balance equation (Brinkman equation) for hydrogen flowing inside the media under laminar flow conditions is expressed as follows:

$$\frac{\rho}{\varepsilon} \frac{\partial \vec{v}_s}{\partial t} + \left(\frac{\mu}{\kappa} + \frac{S}{\varepsilon^2} \right) \vec{v}_s =$$
$$-\nabla P + \nabla \cdot \left[\frac{\mu}{\varepsilon} \left(\nabla \vec{v}_s + \nabla \vec{v}_s{}^T \right) \right] - \nabla \cdot \left[\left(\frac{2\mu}{3} - \eta_d \right) \left(\frac{1}{\varepsilon} \right) (\nabla \cdot \vec{v}_s) \underline{\underline{I}} \right] \qquad (4)$$

with P being the pressure, μ being the dynamic viscosity, and η_d being the dilatational viscosity of the H_2 gas. This equation also includes the viscous stress term expressed in terms of velocity components, taking into account the viscosity of the media as well.

For free flows without porous media (such as the hydrogen connecting tubes and open channels in the tank) the momentum balance equation under laminar conditions is expressed as:

$$\rho \frac{D\vec{v}}{Dt} = -\nabla P - \nabla \cdot \underline{\underline{\tau}} \tag{5}$$

The energy balance of the MH system, comprising the MH material and the hydrogen in gaseous state, is reported at Equation 6:

$$\rho_{MHBulk} C_{MH} \frac{\partial T}{\partial t} - \nabla \cdot \left(k (\vec{\nabla} T) \right) = -\varepsilon \rho_{H2} C_{H2} \left(\frac{\partial T}{\partial t} + \vec{v} \cdot \vec{\nabla} T \right) + \varepsilon \frac{\partial P}{\partial t} + C_{H2} T \cdot S + S \cdot \Delta H \tag{6}$$

with C_{MH} being the specific heat of the MH material, k being the thermal conductivity, and ΔH being the enthalpy of reaction.

The energy balance equation has been assessed imposing the internal energy balance of the overall system and replacing the enthalpy terms with the corresponding Equation 1. Equation 6 is the general energy balance equation in a medium reacting with a fluid. It accounts for pressure work term and viscous dissipation term, yet the terms related to the kinetics energy and to gravitational force work are neglected. This simplifies the solution of the differential equations and reduces the computational time.

For hydrogen flowing into no porous volumes, the energy balance equation is expressed as:

$$c \frac{\partial h}{\partial T} \frac{\partial T}{\partial t} - \nabla \cdot k \nabla T = -c \frac{\partial h}{\partial T} \vec{v} \cdot \nabla T - \frac{T}{c} \frac{\partial c}{\partial T} \left(\frac{\partial P}{\partial t} + \vec{v} \cdot \nabla P \right) - \underline{\underline{\tau}} : \nabla \vec{v} \tag{7}$$

with c being the molar concentration and h the molar enthalpy of hydrogen gas

The model evaluates the hydrogen state adopting Equation 8, with compressibility factor which modifies the ideal gas state equation:

$$P = Z(P,T)\rho RT \tag{8}$$

The compressibility factor has been evaluated, fitting the data available from the NIST database [20].

A first order kinetics expression was adopted to simulate hydrogen absorption/desorption in the HTMH and LTMH materials:

$$\frac{dX}{dt} = \begin{cases} C_a \exp\left(-\dfrac{E_a}{RT}\right) ln\left(\dfrac{P}{P_{eq}}\right)(X_M - X), & P > P_{eq} \\[4mm] C_d \exp\left(-\dfrac{E_d}{RT}\right)\left(\dfrac{P - P_{eq}}{P_{eq}}\right)(X - X_m), & P < P_{eq} \end{cases} \tag{9}$$

with C_a and C_d being the pre-exponential kinetics factors and E_a and E_d being the activation energies for H_2 absorption and desorption respectively and X_M and X_m being respectively the maximum and minimum molar concentrations of H_2 within the MH material. The kinetics parameters are obtained from experimental measurements using MH powders thus implicitly capturing the effects of both the surface reaction kinetics and diffusion rates in the MH particles.

The first expression of Equation 9 represents the hydrogen absorption kinetics at pressures higher than the equilibrium pressure, while the second expression represents the hydrogen desorption kinetics when pressures are lower than the equilibrium pressure.

The equilibrium pressure of the HTMH and LTMH was assessed adopting the van't Hoff equation (Equation 10):

$$P_{eq} = P_{atm} \exp\left(\frac{\Delta H}{RT} - \frac{\Delta S}{R}\right) \tag{10}$$

The current model assumes no slope in the bi-phase region and no hysteresis for the absorption/desorption process. Additional correction factors that will account for these phenomena will be included in the future work when the model results will be validated with experimental results.

2.2   Bench-scale paired MH system

The proposed MH-based system is comprised of Mg_2FeH_6 material as the HTMH, coupled with Na_3AlH_6 material as the LTMH. This system has been modeled using the numerical model described previously. Its parameters, as well as the initial and boundary conditions applied to solve the differential equations, are based on the material properties and on the characteristics of the experimental system available at the Savannah River National Laboratory (SRNL) and Greenway Energy laboratories. The model geometry has been set up based on the experimental MH reactor, as described in the next sections.

2.2.1   Experimental setup and material properties

Figure 1 shows the overall bench scale experimental system (left) and one of the MH test vessels (middle), with the corresponding mathematical model rendering of the reactor.

The bed pairing system allows for the two metal hydrides to be directly tested at operational temperature and pressures. To provide accurate measurements of the pressure change when the beds are paired a differential pressure transducer was installed that is referenced to a calibrated reservoir. The differential pressure transducer was designed for high pressure applications where experimental data collected by a high pressure gauge would not provide enough precision over the full test range. Sample vessels were purchased that can accommodate anywhere from one gram to tens of grams of material. These vessels can operate at moderately high temperatures and pressures. In addition, custom made vessels (not pictured) were designed and built to operate at substantially high temperatures (+800 °C) as well as high pressures (tested up to 100 bar at temperature).
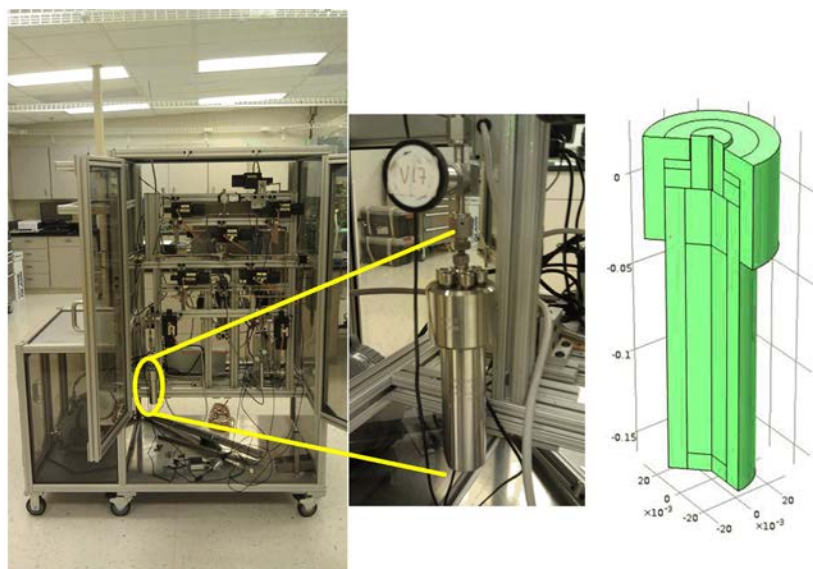
Figure 1. High pressure bench scale apparatus for pairing two metal hydride beds (left), close up of image of one of the metal hydride beds (middle), model rendering of the sample vessel for modeling validation (right).

The system in Figure 1 allows for independent control of the paired bed temperatures as well as aliquots of hydrogen gas to each bed throughout an experiment. With these features, coupled with the software written to control the overall system, the metal hydride beds can be cycled under various operational conditions to best validate the model.

The metal hydrides chosen for the current work are magnesium iron (Mg_2FeH_6) and the hexahydride phase of sodium alanate (Na_3AlH_6). The Mg-Fe hydride would cycle between Mg_2FeH_6, formed when hydrogen is absorbed and the thermal energy is released, and 2Mg + Fe, formed when hydrogen is desorbed with the thermal energy stored in the LTMH. The sodium alanate would cycle between Na_3AlH_6, formed when hydrogen absorbed in the LTMH, and NaH + Al, formed when hydrogen is released by the LTMH and absorbed by the HTMH. The alanate side of the paired system would be run through a temperature swing on the order of 160-180 °C to either absorb or desorb the hydrogen with the Mg-Fe side left at an approximately constant temperature on the order of 450 °C. The stability of the hexahydride material, along with its thermal and physical properties, has been extensively studied. The material demonstrated stable capacities for extended cycling and the capability to reach thermal conductivity values of about 9 W/mK in pelletized form [21,22]. A

change in gas pressure along with a change in temperature to the alanate bed allows for cycling of hydrogen to and from each of the paired metal hydrides.

The two material thermodynamic and physical properties are shown in Table 1. The values of reaction enthalpy and entropy are those reported in References [23-24]. The density values have been calculated based on the crystal density and the bed porosity, assumed equal to 50%. The value of the specific heat and the thermal conductivity of the two materials are typical values for the two selected materials and have been assumed based on the data reported in References [23-24]. The weight capacity of the two materials has been assessed based on the values obtained from PCT and TGA experimental tests carried out at SRNL.

Table 1: Properties of MH powder beds

Property	Units	HTMH	LTMH	
ΔH	J/mol	77000	47000	Reaction enthalpy
ΔS	J/mol·K	137.0	134.85	Reaction entropy
ρ	kg/m^3	1300	750	Bulk density
C_{MH}	J/kg·K	800	800	Specific heat
k_{tot}	W/m·K	0.35	0.35	Overall thermal conductivity of H$_2$-filled MH bed
ϵ		0.5	0.5	Porosity of bed
$wt\%$	kgH2/kgMatl	5.0	1.45	Weight capacity

2.2.2 Numerical model

Each metal hydride requires a heat input during the endothermic H$_2$ discharging process. In a real application, the heat input to the HTMH would be supplied by concentrating solar power during LTMH charging while the heat input to the LTMH during HTMH charging would be supplied by waste heat from the power system or another source of low-grade heat. In the bench-scale experimental setup, the heat input will be supplied by electric heaters providing constant thermal power over the duration of the MH discharging step. In the numerical model, the heat input to each metal hydride is imposed as a uniform volumetric heat source throughout the MH volume. This implementation was chosen to minimize heat transfer limitations associated with heating the metal hydride during the initial concept demonstration.

2.2.2.1   Model geometry

The numerical model geometry consisted of the two stainless steel MH vessels connected by a short tube to

transfer H_2 between them. The two vessels and the connecting tube were aligned along a common axis so that

the overall system was axisymmetric and could be modeled in two dimensions, r and z. Figure 2 shows the 2D

axisymmetric geometry simulated. It was divided into regions of stainless steel, free hydrogen gas, and porous

MH beds consisting of MH powder with hydrogen gas filling the void space between particles. The MH beds

were modeled as homogeneous cylinders with effective properties accounting for the porosity. The powder was

assumed to uniformly fill the vessel cavity up to a specified distance, with free H_2 gas filling the remainder of the

cavity. The geometry of the experimental stainless steel vessels was replicated as closely as possible in the

model, while the connecting tubing was shortened and simplified.
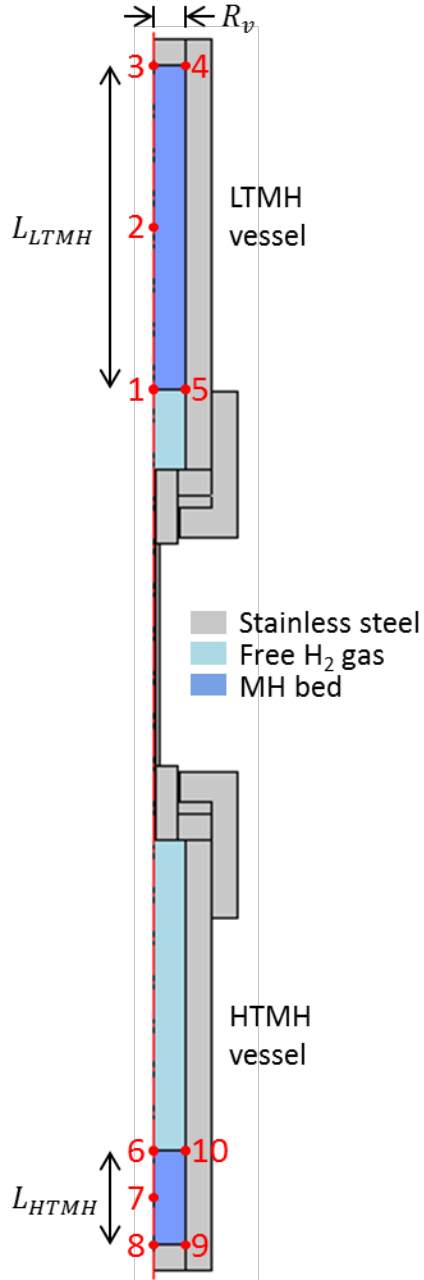
Figure 2: Schematic of 2D axisymmetric model geometry, showing the materials of each component and key dimensions of the MH beds, namely the inner radius R_v of the vessel cavity and the fill lengths L_{LTMH} and L_{HTMH} of the LTMH and HTMH beds, respectively. The 10 numbered locations within the LTMH and HTMH beds are those where local temperatures and equilibrium pressures will be plotted.

2.2.2.2 Boundary and initial conditions

The energy conservation equations (6-7) governing the temperature T are first order in time and second-order in space. Therefore, they require one initial condition and two boundary conditions for the temperature T in each direction. The kinetics equations (9) governing the absorbed hydrogen concentration X inside each metal

hydride are first order in time, so they require one initial condition within each MH volume. The mass conservation equations (1) and (3) (first-order in time and space) and the momentum equations (4-5) (first order in time and second-order in space), governing the pressure P and gas velocity $\vec{v}$ require one initial condition and two boundary conditions in each direction.

Initially, the temperature T of the entire HTMH vessel, including both the stainless steel and the MH material and H_2 contained inside, is uniform and equal to $T_{0,HTMH} = 450°C$. Similarly, the initial temperature of the LTMH vessel is uniform and equal to $T_{0,LTMH} = 160°C$. The temperature along the tube connecting the two vessels varies linearly in the z-direction from $T_{0,HTMH}$ at the bottom to $T_{0,LTMH}$ at the top. The absorbed hydrogen concentration X within each MH bed was initially uniform and equal to $X_{,0,HTMH} = 0.95\,X_{,M,HTMH}$ and $X_{,0,LTMH} = 0.05\,X_{,M,LTMH}$ in the HTMH and the LTMH, respectively. Here, the total amount of hydrogen initially absorbed in the metal hydrides equals the maximum capacity n_M of either MH bed. The gas pressure was initially uniform throughout the entire system and equal to the equilibrium pressure of the HTMH, i.e., $P_{eq,0} = P_{eq,HTMH}(T_{0,HTMH})$, while the gas velocity $\vec{v}$ was zero everywhere.

Because the system is axisymmetric and solved in two dimensions, boundary conditions are required only in the radial r and axial z-directions. At the system centerline $r = 0$, axial symmetry existed for all variables, i.e., $\partial T/\partial r\ (r = 0) = 0$, $\partial P/\partial r\ (r = 0) = 0$, and $u_r(r = 0) = 0$. No slip and no penetration boundary conditions existed for the H_2 gas on all inside walls of the vessel at all times, i.e., $\vec{v}|_{wall} = \mathbf{0}$ and $\nabla P|_{wall} = 0$. The cap of each vessel and the connecting tube were thermally insulated on their outer surfaces at all times. During discharging of each metal hydride, the entire outer surface of the vessel was thermally insulated while a volumetric heat source was applied to the MH bed. During charging of the metal hydride, a constant and uniform temperature, equal to $T_{0,HTMH}$ and $T_{0,LTMH}$ for the HTMH and LTMH vessels, respectively, was imposed on the outer wall and bottom of the vessel.

2.2.2.3   Sizing of the coupled MH bench scale system

To avoid excess cost and system volume, the MH volumes should be selected so that the H_2 storage capacities of the two MH beds are the same. The theoretical maximum H_2 storage capacity $n_{M,i}$ of a MH bed (in mol H_2), where $i = HTMH$ or $i = LTMH$, can be computed from its maximum H_2 concentration $X_{H_2,M,i}$ and its volume as $n_{M,i} = X_{H_2,M,i}(\pi R_v^2 L_i)$, where R_v is the radius of the MH cavity and L_i is the fill length of the metal hydride in the cavity. Setting the theoretical capacities of both MH beds equal so that $n_M = n_{M,HTMH} = n_{M,LTMH}$ yields the following expression relating their volumes:

$$L_{LTMH} = \left(\frac{X_{,M,HTMH}}{X_{,M,LTMH}}\right) L_{HTMH} \qquad (11)$$

For the metal hydrides modeled in the present study, the LTMH is 3.47 times larger than the HTMH. To maintain a free gas space in each cavity equal to at least 20% of the cavity volume, the LTMH volume was set to $L_{LTMH} = 0.8L_v = 0.122$ m. This results in a theoretical H_2 storage capacity of $n_M = 0.561$ mol for the system, and a HTMH fill length of $L_{HTMH} = 0.0352$ m.

The heater power supplied to each MH bed during H_2 discharging must be selected to (1) provide sufficient thermal energy to completely discharge the MH bed and (2) minimize wasted energy input and undesirable temperature rise.

For each metal hydride, the thermal energy $Q_{rxn,i}$ (in J) required by the endothermic desorption reaction to discharge the full H_2 capacity (n_M) can be computed based on the enthalpy of reaction ΔH_i as $Q_i = n_M \Delta H_i$. For the MH materials and system capacity of the present model, the required thermal energies are $Q_{rxn,LTMH} = 26.388$ kJ and $Q_{rxn,HTMH} = 43.231$ kJ.

The values of $Q_{rxn,i}$ correspond to the thermal energy inputs required for the desorption reaction only. In order to transfer H_2 between the paired MH beds, a drop in equilibrium pressures between the discharging metal hydride and the charging metal hydride is also required. Therefore, changing the direction of H_2 flow requires

one or both of the MH beds to change temperature, and additional thermal energy input is required for this sensible heating. For a thermal storage application, the HTMH ideally remains at a constant temperature determined by requirements of the power cycle while the LTMH varies in temperature as required to drive H_2 flow. The thermal energy input required to raise the temperature of the LTMH and its stainless steel (SS) vessel by a temperature difference ΔT can be computed as $Q_{LTMH,\Delta T} = \rho_{LTMH} V_{LTMH} C_{LTMH} \Delta T$ and $Q_{SS,\Delta T} = \rho_{SS} V_{SS} C_{SS} \Delta T$, respectively, where ρ_i, V_i, and C_i are the density, volume, and specific heat of material i.

Here, the HTMH set point is 450°C, based on a suitable range of input temperature for a steam power cycle. Assuming uniform temperature within both MH beds, the system would be in equilibrium when the LTMH temperature is 177°C, i.e., $P_{eq,HTMH}(450°C) = P_{eq,LTMH}(177°C)$ (Equation 10). During LTMH charging, the LTMH surface temperature is fixed almost 20°C lower at $T_{0,LTMH} = 160°C$ to lower its equilibrium pressure relative to the HTMH. Then, during HTMH charging, the LTMH temperature must exceed 177°C to raise its equilibrium pressure above that of the HTMH. Here, we assume that the LTMH must reach approximately 200°C during HTMH charging, meaning the heater must raise temperature of the LTMH and its vessel by $\Delta T = 40°C$ between the LTMH charging and the HTMH charging steps. The required sensible heat inputs are $Q_{LTMH,40°C} = 1.437$ kJ and $Q_{SS,40°C} = 45.882$ kJ. The small scale of the system results in a large ratio of stainless steel to MH volume and, consequently, an exorbitantly large fraction of the energy input contributes to heating the stainless steel vessel rather than the metal hydride itself. This fraction should shrink significantly as the system is scaled up for practical implementation.

The thermal energy input to each MH bed is provided as a constant thermal power input $\dot{Q}_{h,i}$ over the 1.5 h discharging step, i.e., $\dot{Q}_{h,HTMH} = Q_{rxn,HTMH}/(1.5 \text{ h}) = 8.01$ W and $\dot{Q}_{h,LTMH} = (Q_{rxn,LTMH} + Q_{LTMH,40°C} + Q_{SS,40°C})/(1.5 \text{ h}) = 13.65$ W. The thermal power $\dot{Q}_{h,i}$ is distributed uniformly throughout the MH volume, so that local heater powers for the HTMH and the LTMH are $\dot{q}_{h,HTMH} = \dot{Q}_{h,HTMH}/(\pi R_v^2 L_{HTMH}) = 463$ kW/m^3 and $\dot{q}_{h,LTMH} = \dot{Q}_{h,LTMH}/(\pi R_v^2 L_{LTMH}) = 228$ kW/m^3, respectively.

3   Results and Discussion

3.1   Individual MH characterization

3.1.1   MH absorption/desorption kinetics under constant temperature and pressure

A first order kinetics expression has been adopted to simulate the absorption/desorption of hydrogen both in the HTMH (Mg_2FeH_6) and in the LTMH (Na_3AlH_6). The kinetics parameter values are reported in Table 2.

Table 2: Kinetics parameters for the HTMH (Mg_2FeH_6) and LTMH (Na_3AlH_6) materials

	HTMH (Mg_2FeH_6)	LTMH (Na_3AlH_6)
Ca (1/s)	10000	8E+5
Ea (J/molH_2)	70000	70000
Cd (1/s)	12000	5E+12
Ed (J/molH_2)	90000	118600
X_M (molH_2/m^3)	32468	5400
X_m (molH_2/m^3)	0	0

The LTMH material parameters were assumed based on References [24-25]. The HTMH material parameters were assessed using MathCad® optimization tool to match the available experimental data. Because the kinetics parameters were fitted from data for MH powders, these values account for the effects of factors such as particle size distribution without explicit inclusion of powder properties in the model. The assumed kinetics parameters are expected to be broadly applicable for as-produced Mg_2FeH_6 and Na_3AlH_6 powders since the typical production processes of such metal hydrides produce a consistent powder. HTMH absorption and desorption tests have been carried out at SRNL at temperature of 450 °C and pressure of 50 bar and 500 °C and 1 bar respectively. The values of the activation energy were measured experimentally, while the other kinetics parameters were assessed fitting the experimental data. Results are reported in Figures 3-5.
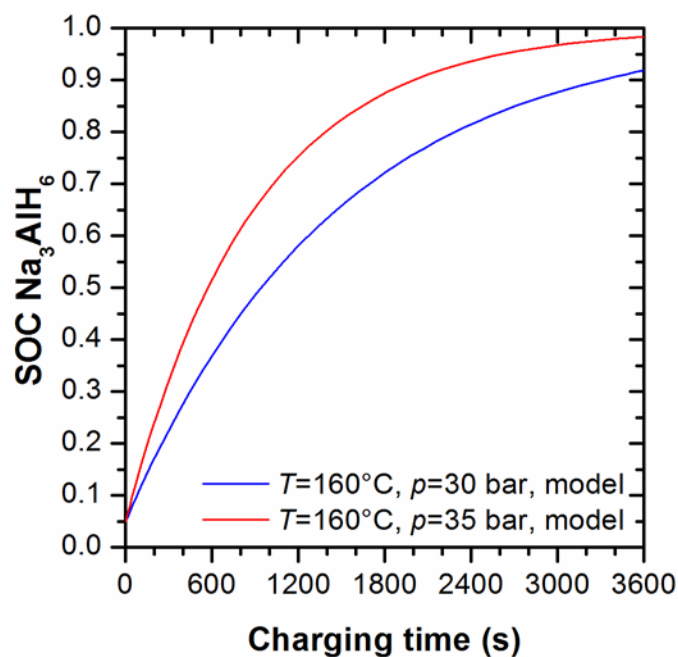
Figure 3: Modeling SOC results for LTMH (Na3AlH6) hydrogen absorption kinetics at temperature of 160 °C and pressures of 30 bar and 35 bar
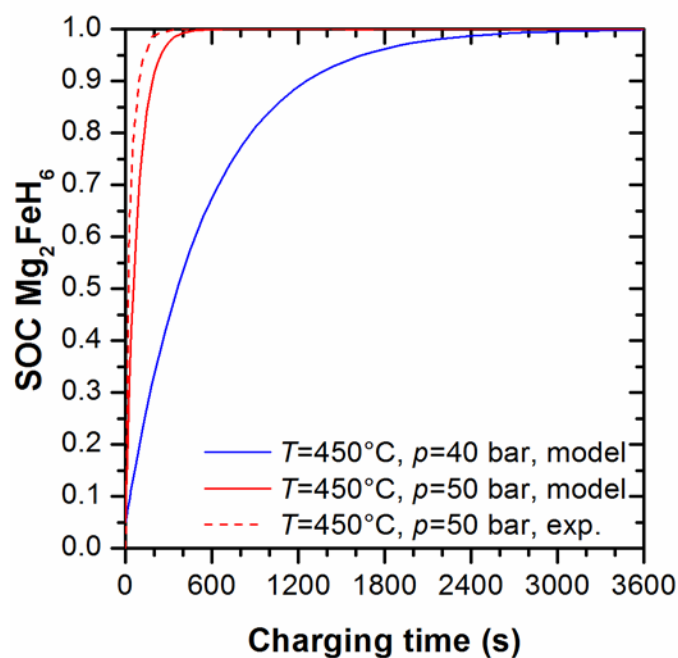

Figure 4: Modeling ('model') and experimental ('exp') SOC results for HTMH (Mg2FeH6) hydrogen absorption kinetics at temperature of 450 °C and pressures of 40 bar and 50 bar
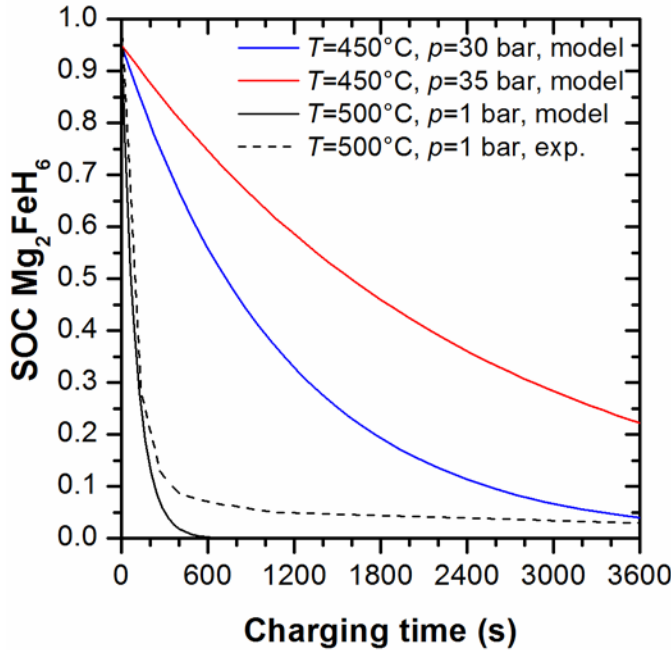
Figure 5: Modeling ('Mod') and experimental ('Exp') SOC results for HTMH (Mg2FeH6) hydrogen desorption kinetics at temperature of 450 °C and 500 °C and pressures of 1 bar, 30 bar and 35 bar

Figure 3 shows the numerical model hydrogen absorption results in the LTMH material at temperature of 160 °C and pressures of 30 bar and 35 bar. Figure 4 and Figure 5 show the absorption and desorption profiles in the HTMH at different pressures and temperatures. The numerical model results are in good agreement with the corresponding experimental data available from the SRNL tests as shown in Figures 4 and 5.

3.2   Model results for bench-scale paired MH system

The bench-scale paired MH system was simulated for ten full cycles consisting of a LTMH charging step and a HTMH charging step. By the third cycle, the system reached a steady cycling condition (i.e. the relative differences in the gas pressure and in the local temperature and H_2 concentration between time t and time $t +$ 1.5 h was less than 2%). Therefore, the results are plotted for the first three cycles in order to show both the start-up effects due to the initial conditions and the steady cycling behavior. The performance of the system is assessed using overall values obtained from spatial integration over volumes and surface areas of the system. Local temperatures and pressures are plotted at selected locations 1-10 identified in Figure 2 to illustrate the spatial distribution resulting from the system's heat transfer characteristics. The five locations selected in each

MH include the center point on the interface between the MH and the free H_2 gas, the centroid of the MH bed, and several locations along the interface between the MH and the vessel.

3.2.1 Model temperature profiles

Figure 6 shows local temperatures as a function of time for (a) five locations within the LTMH and (b) five locations within the HTMH, as well as the average temperature $\bar{T}$ of each MH bed. Figure 6(a) shows that the temperatures within the LTMH ranged from about 160°C to 235°C. During LTMH charging, the temperatures of the LTMH at locations in contact with the vessel (T_3, T_4, and T_5) were equal to the temperature imposed on the outer surface of the vessel, $T_{0,LTMH} = 160°C$. Meanwhile, the temperatures inside the LTMH (T_1 and T_2) and the average $\bar{T}_{LTMH}$ were higher due to the heat released internally by H_2 absorption. During the HTMH charging step, the LTMH average and centerline temperatures increased rapidly for approximately one minute until the maximum temperature T_2 at the center of the LTMH reached approximately $180°C$. Then, all LTMH temperatures continued to increase at a significantly slower rate. The abrupt decrease in $\partial T/\partial t$ can be attributed to the onset of H_2 desorption, which consumed a significant portion of the thermal energy supplied by the heater. The average LTMH temperature $\bar{T}_{LTMH}$ reached a maximum of about 220°C during the HTMH charging step, about 20°C higher than accounted for by the heater power calculations in Section 2.4.2. This additional sensible heating suggests that less than the full H_2 capacity n_M was discharged from the LTMH, so that the reaction absorbed less thermal energy than calculated.

Starting in the second cycle, there was a temperature drop in the LTMH at the beginning of the LTMH charging step. This can be attributed to the imposed temperature boundary condition on the outer surface of the vessel. The instantaneous transition from thermal insulation with volumetric heating to an imposed temperature of 160℃ on the vessel surface is an idealized boundary condition corresponding to an infinitely large heat transfer coefficient at this boundary. In actual experiments, the vessels will be cooled by convection in air, with heaters preventing the temperature from dropping below the set point. As a result, the heat flux exiting the vessel will

be limited by the thermal resistance between the vessel surface and the ambient air, which will result in a slower cooling period than that simulated.
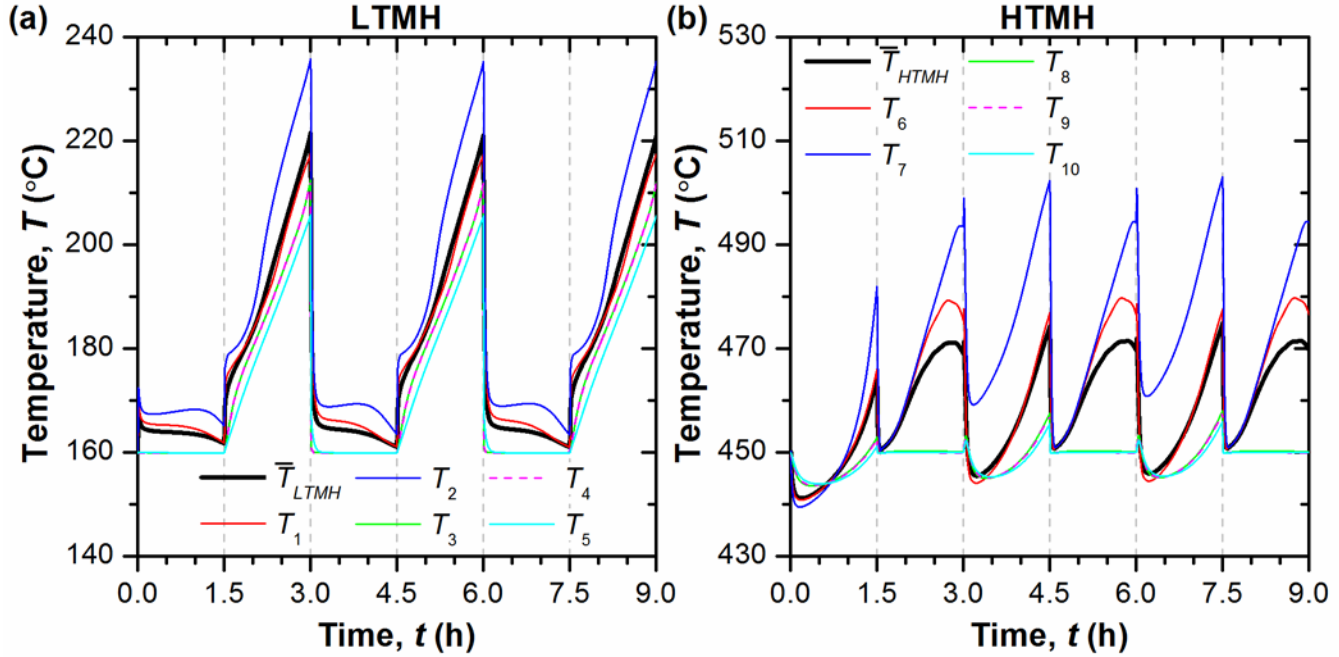

Figure 6: Local temperature as a function of time for (a) five locations within the LTMH and (b) five locations within the HTMH, as well as the average temperature of each MH, as functions of time. The HTMH remained within about +55/-10°C of the desired setpoint of 450°C, while the LTMH remained within about +75°C of its initial temperature of 160°C.

Figure 6(b) shows that the maximum and minimum temperatures in the HTMH remained within about +55/-10°C of the targeted temperature of 450°C. As observed for the LTMH, the temperatures at locations in contact with the vessel (T_8, T_9, and T_{10}) were systematically lower than those along the centerline (T_6 and T_7) or the average $\bar{T}_{HTMH}$ due to the volumetric heating. In fact, the temperatures on the outer MH surface (T_8, T_9, and T_{10}), remained within the much smaller temperature range 450°C±10°C.

3.2.2 Model pressure profiles

Figure 7 shows the pressure P of the H$_2$ gas in the system and the average equilibrium pressures $\bar{P}_{eq,HTMH}$ and $\bar{P}_{eq,LTMH}$ of the HTMH and the LTMH, respectively, as functions of time. The pressure P was approximately uniform throughout the gas. The spatial pressure variations required to drive the gas between the vessels were negligibly small (≤100 Pa) compared to the temporal changes or the difference $P_{eq,i} - P$ required to drive the

absorption/desorption reactions. The system pressure varied over a range of approximately 5 MPa, from $\min(P) \approx 3$ MPa early in the LTMH charging step to a maximum of $\max(P) = 8$ MPa at the end of the HTMH charging step. The 5-MPa decrease occurred rapidly, within approximately the first 10 minutes of the LTMH charging step, and P increased monotonically through the rest of the LTMH charging and HTMH charging steps.

The continuous variation of MH temperatures (Fig. 6) resulted in continuously changing equilibrium pressures, as described by Equation 10. Here, $\bar{P}_{eq,HTMH}$ varied over a relatively narrow range of 4–6 MPa, consistent with the relatively small variation of the HTMH average temperature. By contrast, $\bar{P}_{eq,LTMH}$ dropped to about 2.5–3 MPa during LTMH charging steps and increased to 12 MPa during HTMH charging steps in order to drive the H_2 flow between the two vessels. In other words, large changes in the average equilibrium pressure of the LTMH enabled a relatively stable operation of the HTMH over the entire cycle. The predicted range of system pressure is large but within the operating range of the current experimental system, which is rated for pressures as high as 10 MPa.
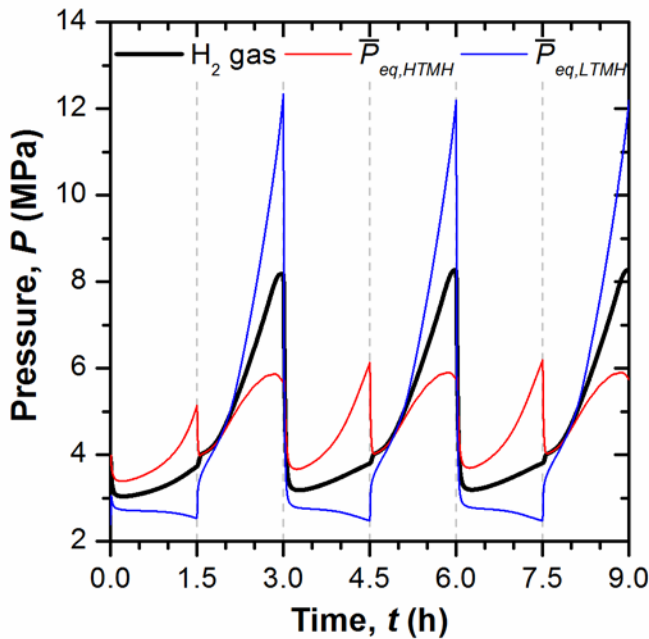

Figure 7: Pressure P of the hydrogen gas and average equilibrium pressures $\bar{P}_{eq,HTMH}$ and $\bar{P}_{eq,LTMH}$ for the HTMH and LTMH, respectively, as functions of time over three cycles. The pressure was nearly uniform throughout the gas, and was roughly halfway between the values of $\bar{P}_{eq,LTMH}$ and $\bar{P}_{eq,HTMH}$ for most of the cycle.

Figure 8 shows the local equilibrium pressures P_{eq} at (a) five locations within the LTMH and (b) five locations within the HTMH as functions of time, as well as the gas pressure P in the system. Due to the temperature dependence of P_{eq} (Equation 10), the shapes of the P_{eq} curves closely resemble those of the temperatures at the same locations. At the beginning of the HTMH charging step, the equilibrium pressure $P_{eq,2}$ at the center of the HTMH displays a very rapid increase followed by an abrupt decrease in slope, similar to that previously observed for temperature T_2 (Figure 6). Here, it is evident that the temperature T_2 exceeding $\approx 180°C$ resulted in $P_{eq,2}$ exceeding the gas pressure P. As a result, the H₂ desorption reaction in the LTMH started at this time. The equilibrium pressure was consistently higher at locations along the centerlines of the MH beds (Locations 1-2 in the LTMH and 6-7 in the HTMH) than at locations in contact with the vessel due to the higher internal temperatures caused by internal volumetric heating. This suggests that the H₂ absorption processes would start at the outside of the metal hydride where the difference $P - P_{eq}$ is maximum while the H₂ desorption processes would start in the center of the metal hydride where the difference $P_{eq} - P$ is maximum. In fact, during the HTMH charging step, the equilibrium pressure at the outer surface of the LTMH remained below the gas pressure P, making H₂ desorption at these locations impossible, until the very end of the step.
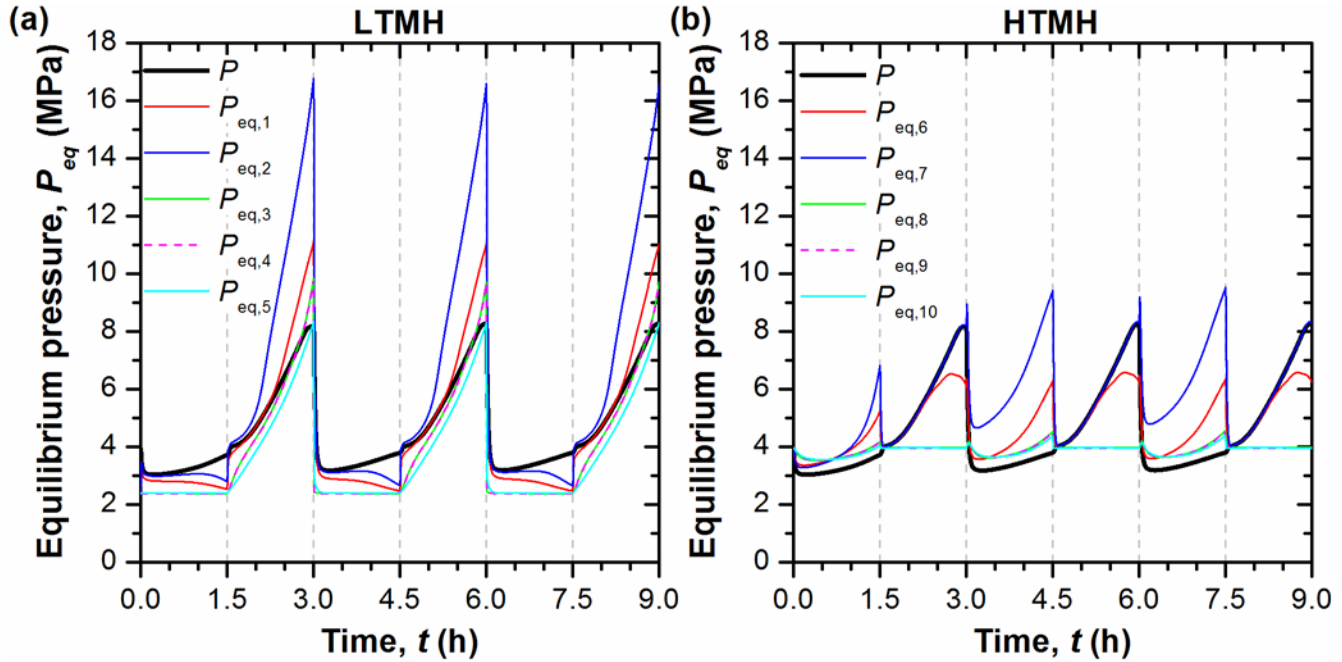
Figure 8: Equilibrium pressures $P_{eq}(r,t)$ as functions of time for (a) five locations in the LTMH and (b) five locations in the HTMH, as well as the gas pressure for the system.

3.2.3 Hydrogen transport and MH state of charge (SOC)

Figure 9(a) shows the molar flowrate of H_2 from the MH bed into the free H_2 volume for each metal hydride as a

function of time. Thus, positive flowrate values result from H_2 desorption from the metal hydride and negative

values from H_2 absorption in the metal hydride. At the beginning of the LTMH charging steps, the flow rate of H_2

exiting the HTMH rapidly increases to a maximum, accompanied by an immediate, even higher flow rate into the

LTMH. The rapid influx of H_2 to the LTMH can be attributed to its abrupt decrease in temperature [Figure 6(a)]

as the imposed temperature of 160°C is applied at the outside of the vessel. This temperature decrease lowers

the LTMH equilibrium pressure below the gas pressure in the system [Figure 8(a)] so that the LTMH begins to

absorb H_2. Since the rate of H_2 absorption in the LTMH is initially much larger than the rate of desorption from

the HTMH (by a factor of about 3.5), the pressure of the H_2 gas drops rapidly until the flowrate out of the HTMH

and into the LTMH become equal. This variation in pressure, driven by the LTMH temperature, is what enables

the HTMH to absorb and desorb H_2 within a relatively small temperature window.

At the beginning of the HTMH charging step, the H_2 flowrates out of the LTMH and into the HTMH increase relatively slowly. This can be attributed to the fact that the constant thermal power supplied to the LTMH by the heater must raise the LTMH temperature enough for its equilibrium pressure to exceed the gas pressure. Because the HTMH surface temperature remains in the narrow range 450°C±10°C [Figure 6(b)], the rapid cooling associated with the imposed temperature boundary condition does not drive significant H_2 absorption in the HTMH. Instead, the H_2 flow remains primarily regulated by the LTMH temperature in both steps of the cycle.

In both steps of the cycle, the flowrate decreases towards the end of the cycle. This can be attributed to H_2 depletion in the metal hydride that is desorbing H_2 [Figure 9(b)].
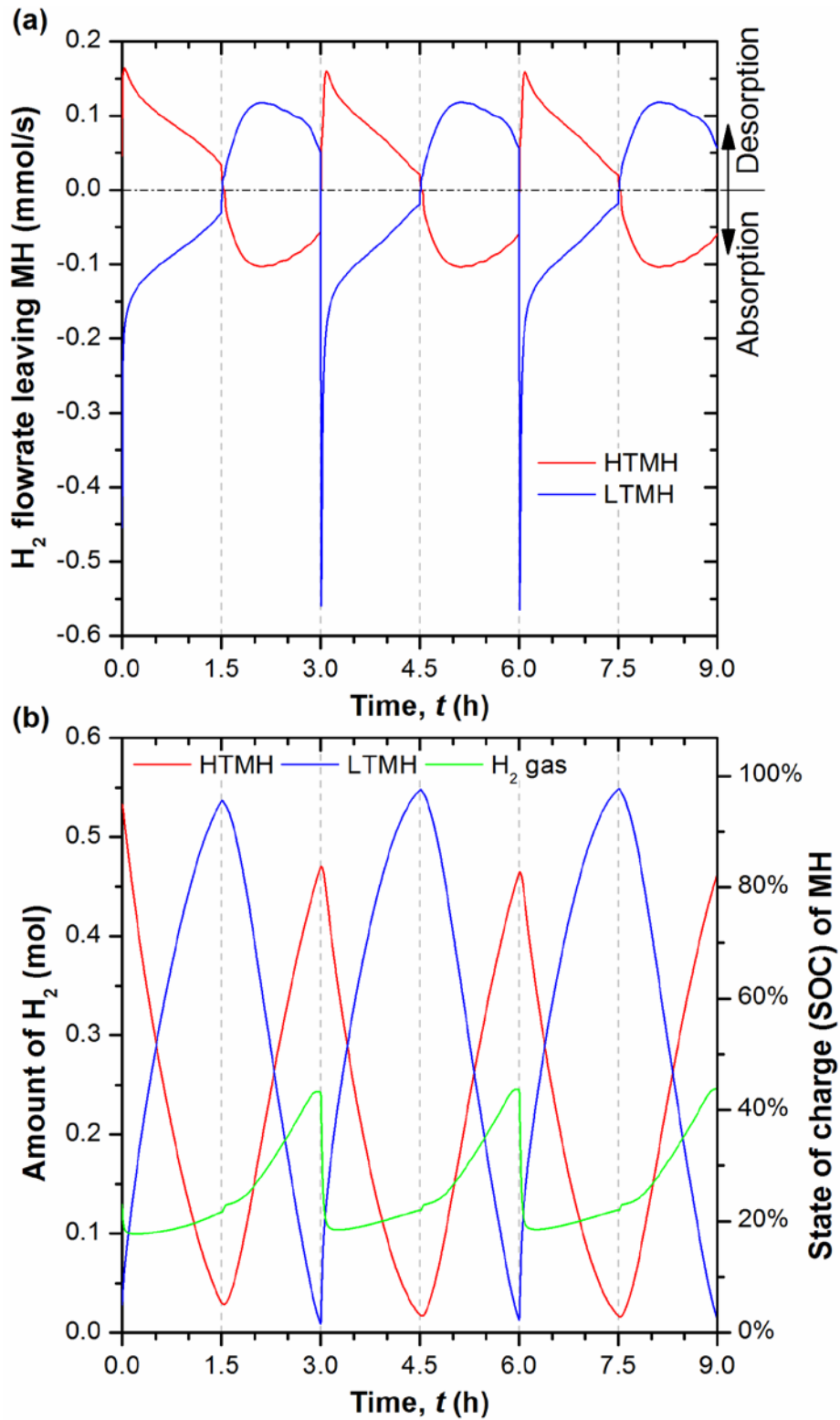
Figure 9: (a) The molar flowrate of H_2 exiting each MH and (b) the amount of H_2 stored in the HTMH, LTMH, and in gaseous form as functions of time. The corresponding state of charge of the MH is shown on the right-hand axis of (b). Eighty percent of the MH H_2 capacity was successfully cycled between the two MH beds. A significant amount of H_2, ranging from 20 to 40% of the MH storage capacity n_M, was in gaseous form.

Figure 9(b) shows the amount of H$_2$ (in mol) stored in the HTMH, the LTMH, and as gas as functions of time. The right-hand scale shows the state of charge (SOC), i.e., the percentage of the MH bed's maximum H$_2$ storage capacity, corresponding to the quantity on the left-hand scale. Eighty percent of the systems maximum storage capacity n_M was successfully cycled in and out of the HTMH. Interestingly, over 95% of the capacity n_M is cycled in and out of the LTMH. The difference between the amount of H$_2$ desorbed by the LTMH and that absorbed by the HTMH is taken up by the gas phase due to the large pressure increase over the cycle (Figure 7). Since the pressure changes play an important role in driving the flow of H$_2$ while maintaining the target HTMH temperature, this suggests that approaching 100% cycling of the HTMH storage capacity would require oversizing the capacity of the LTMH relative to that of the HTMH. In addition, the excess LTMH capacity required to accommodate a given change in pressure would increase with the volume of H$_2$ gas in the system, so the amount of free gas volume should be minimized.

3.2.4 System energy density

Figure 10 shows the heat input from the heater to the HTMH during LTMH charging and the heat output from the HTMH to the vessel during HTMH charging as functions of time. The time-averaged value of the heat output is also plotted. The very small thermal output at the beginning of the HTMH charging step corresponds to the period of relatively small H$_2$ flowrate into the HTMH [Figure 9(a)] associated with raising the LTMH temperature. The decrease in thermal output towards the end of the step corresponds to the decrease in H$_2$ flowrate associated with H$_2$ depletion in the LTMH.

About 83% of the heat input during HTMH discharging was recovered during HTMH charging. The output energy density was $\frac{E_{HTMH,out}}{V_{HTMH}+V_{LTMH}} = 132 \frac{\text{kWh}}{\text{m}^3}$ where $E_{HTMH,out}$ is the total thermal energy output over the HTMH charging step and V_{HTMH} and V_{LTMH} are the volumes of the MH beds (excluding the vessels). This energy density is about 5.3 times the SunShot target of 25 kWh/m^3.
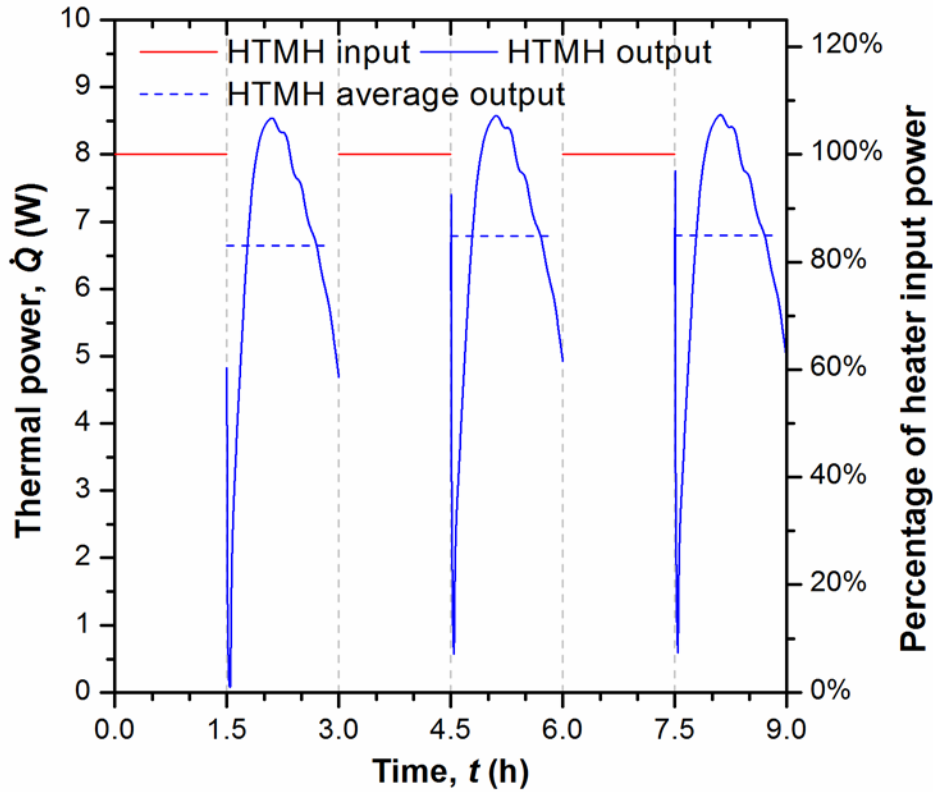
Figure 10: Heat input from heater to HTMH during LTMH charging and heat output from HTMH to vessel during HTMH charging as functions of time, as well the time-averaged heat output. About 83% of the heat input during LTMH charging was returned during HTMH charging.

3.2.5 Influence of cooling boundary condition

As previously noted, the use of imposed temperature boundary conditions to cool the vessels during H_2 absorption resulted in very rapid changes in temperature, pressure, and H_2 flowrate at the beginning of the LTMH charging steps. To assess whether these idealized boundary conditions are a reasonable approximation, the imposed temperature boundary condition was replaced by a convection boundary condition $q''(\boldsymbol{r}, t) = h[T(\boldsymbol{r}, t) - T_a]$ with heat transfer coefficient $h = 10$ W/(m²·K) and ambient temperature $T_a = 20°C$ as long as the surface temperature remained larger than the setpoint (160°C for the LTMH vessel and 450°C for the HTMH vessel).

As expected, the convection boundary condition resulted in a longer cooling period. With convective cooling, the LTMH in contact with the vessel (locations 3–5) required approximately 25 minutes to cool to 160℃. However, despite the large increase in cooling time, the predicted amount of H_2 transferred between the metal

hydrides and the predicted HTMH output energy density were within 3% of the values predicted using the imposed temperature boundary condition. In addition, the temporal evolution of the MH temperatures, gas and equilibrium pressures, and absorbed H_2 concentrations were similar in shape and magnitude for both boundary conditions. This suggests that the overall cycling performance was not very sensitive to the initial cooling rate of the metal hydrides and that the imposed temperature boundary condition is a reasonable first approximation. A more accurate boundary condition should be used if the temporal evolution at the beginning of each step is of interest.

4   Summary and conclusions

A detailed transport model has been set up to evaluate the technical feasibility of solar thermal energy storage systems based on metal hydride materials. The model is comprised of mass, energy and momentum balance equations, integrated with suitable kinetics expressions developed for the specific coupled MH system. The TES system, examined in the current work, is comprised of Mg_2FeH_6 as the HTMH, coupled with Na_3AlH_6 as the LTMH. The selected solar TES stores and releases the thermal energy at temperatures on the order of 450-500 °C. The system has been modeled with geometry and boundary and initial conditions based on the characteristics of the experimental MH reactor available at SRNL and GreenWay Energy laboratories and on the experimental heating and cooling conditions. Results showed the technical feasibility of the system, with adequate hydrogen transfer from the HTMH to the LTMH during the thermal energy storage process and from the LTMH to the HTMH to release the energy previously stored. The operating temperatures of the HTMH ranged from 450 °C to 500 °C making the TES system suitable for pairing with a steam power plant. The LTMH works at temperatures on the order of 160-180 °C and operating pressures ranging from 30 bar up to about 70 bar. The proposed TES system showed an excellent cycling performance of the two MH beds reaching almost complete charging/discharging of the two metal hydrides under the selected operating conditions for multiple

cycles. In practice, this can easily be achieved including a suitable regenerative heat transfer system that allows recovering the sensible heat associated with the hydrogen transferred between the HTMH and LTMH.

The numerical results, obtained for the selected experimental configuration, showed an actual system volumetric energy density of about 132 kWh/m^3, which is more than 5 times larger than the U.S. Department of Energy SunShot target (25 kWh/m^3). The laboratory scale system also showed a good energy efficiency (in terms of ratio between the released thermal energy and the stored thermal energy) of about 83%. This represents a very appealing result, obtained for a small scale laboratory device that includes large thermal masses (e.g. stainless steel walls and reactor caps). The same TES concept, designed and built for a large scale solar power plant, would easily achieve projected large scale efficiencies close to 100%.

5   Acknowledgements

6   References

[1]   Website: http://www.nrel.gov/docs/fy10osti/48658.pdf [accessed January 2017].

[2]   Gil A, Medrano M, Martorell I, Lazaro A, Dolado P, Zalba B, et al. State of the art on high temperature thermal energy storage for power generation. Part 1 - Concepts, materials and modellization. Renewable and Sustainable Energy Reviews 2010;14:31-55.

[3]   Stekli J, Irwin L, Pitchumani R. Technical challenges and opportunities for Concentrating Solar Power with Thermal Energy Storage. Journal of Thermal Science and Engineering Applications 2013;5:021011-1-12.

[4]   Izquierdo S, Montanes C, Dopazo C, Fueyo N. Analysis of CSP Plants for the Definition of Energy Policies: The Influence on Electricity Cost of Solar Multiples, Capacity Factors and Energy Storage. Energy Policy 2010;38(10):6215-6221.

[5]   Denholm P, Hand M. Grid Flexibility and Storage Required to Achieve Very High Penetration of Variable Renewable Electricity. Energy Policy 2011;39(3):1817-1830.

[6]   Dominguez R, Baringo L, Conejo A. Optimal strategy for a concentrating solar power plant. Applied Energy 2012;98:316-325.

[7]   Corgnale C, Hardy BJ, Motyka T, Zidan R, Teprovich J, Peters B. Screening analysis of metal hydride based thermal energy storage systems for concentrating solar power plants. Renew Sustain Energy Rev 2014;38:821-833.

[8]   Corgnale C, Hardy B, Motyka T, Zidan R. Metal hydride based thermal energy storage system requirements for high performance concentrating solar power plants. Int J Hydrogen Energy 2016;41(44):20217-20230.

[9]   Ward P, Corgnale C, Teprovich J, Motyka T, Hardy B, Peters B et al. High performance metal hydride based thermal energy storage systems for concentrating solar power applications" Journal of Alloys and Compounds 2015;645(1):S374-S378.

[10]   Bogdanović B, Ritter A, Spliethoff B. Active MgH2-Mg systems for reversible chemical energy-storage. Angewandte Chemie-International Edition in English 1990;29(3):223-234.

[11]   Bogdanović B, Ritter A, Spliethoff B, Straßburger K. A process steam generator based on the high temperature magnesium hydride/magnesium heat storage system. Int. J. Hydrogen Energy 1995;20:811-822.

[12]   Bogdanović B, Hartwig TH, Spliethoff B. The development, testing and optimization of energy-storage materials based on the MgH2-Mg systems. Int. J. Hydrogen Energy 1993;18(7):575-589.

[13]   Reiser A, Bogdanović B, Schlichte K. The application of Mg-based metal-hydrides as heat energy storage systems. Int. J. Hydrogen Energy 2000;25:425-430.

[14]   Sheppard D, Corgnale C, Hardy B, Motyka T, Zidan R, Paskevicious M, et al. Hydriding characteristics of NaMgH2F with preliminary technical and cost evaluation of magnesium-based metal hydride materials for concentrating solar power thermal storage. RSC Advances 2014;4:26552-26562.

[15]   Ward PA, Corgnale C, Teprovich JA, Motyka T, Hardy B, Sheppard D, et al. Technical challenges and future direction for high efficiency metal hydride thermal energy storage systems. Applied Physics A 2016;122:462.

[16]   Sheppard DA, Paskevicius M, Humphries TD, Felderhoff M, Capurso G, Bellosta von Kolbe J, et al. Metal hydrides for concentrating solar thermal power energy storage. Applied Physics A 2016;122:395.

[17]   Corgnale C, Hardy B, Anton D. Structural analysis of metal hydride-based hybrid hydrogen storage systems. Int. J. Hydrogen Energy 2012;37(19):14223-14233.

[18]   Corgnale C, Motyka T, Greenway S, Perez-Berrios J, Nakano A, Ito H, et al. Metal hydride bed system model for renewable source driven Regenerative Fuel Cell. J. of Alloys and Compounds 2013;580(1):S406-S409.

[19]   Nakano A, Ito H, Maeda T, Munakata T, Motyka T, Corgnale C, et al. Study on a metal hydride tank to support energy storage for renewable energy. J. of Alloys and Compounds 2013;580(1):S418-S422.

 [20]   Website: http://webbook.nist.gov/chemistry/fluid/ [accessed November 2016].

[21]   Sulic M, Cai M, Kumar S. Cycling and engineering properties of highly compacted sodium alanate pellets. Int J Hydrogen Energy 2012;37(20):15187-15195.

[22]   Sulic M, Cai M, Kumar S. Controlled degradation of highly compacted sodium alanate pellets. Int J Hydrogen Energy 2013;38(7):3019-3023.

[23]   Corgnale C, Hardy BJ, Tamburello DA, Garrison SL, Anton DL. Acceptability envelope for metal hydride-based hydrogen storage systems. Int J Hydrogen Energy 2012;37(3):2812-2824.

[24]   Hardy BJ, Anton DL. Hierarchical methodology for modeling hydrogen storage systems. Part I: Scoping models. Int J Hydrogen Energy 2009;34(5):2269-2277.

[25]   Hardy BJ, Anton DL. Hierarchical methodology for modeling hydrogen storage systems. Part II: Detailed models. Int J Hydrogen Energy 2009;34(7):2992-3004.